ChemPubSoc Europe

DOI: 10.1002/cmdc.201900620

CHEMMEDCHEM Full Papers

Special Collection

Self-Assembly and Neurotoxicity of β-Amyloid (21–40) Peptide Fragment: The Regulatory Role of GxxxG Motifs

Dibakar Sarkar,[a] Ipsita Chakraborty,[a] Marcello Condorelli,[b] Baijayanti Ghosh,[c] Thorben Mass,[d] Markus Weingarth,[d] Atin K Mandal,[c] Carmelo La Rosa,*[b] Vivekanandan Subramanian,*[e] and Anirban Bhunia*[a]

The three GxxxG repeating motifs from the C-terminal region of β-amyloid (Aβ) peptide play a significant role in regulating the aggregation kinetics of the peptide. Mutation of these glycine residues to leucine greatly accelerates the fibrillation process but generates a varied toxicity profile. Using an array of biophysical techniques, we demonstrated the uniqueness of the composite glycine residues in these structural repeats. We used solvent relaxation NMR spectroscopy to investigate the role played by the surrounding water molecules in determining the corresponding aggregation pathway. Notably, the conformational changes induced by Gly^{33} and Gly^{37} mutations result in significantly decreased toxicity in a neuronal cell line. Our results indicate that $G^{33}xxxG^{37}$ is the primary motif responsible for Aβ neurotoxicity, hence providing a direct structure–function correlation. Targeting this motif, therefore, can be a promising strategy to prevent neuronal cell death associated with Alzheimer's and other related diseases, such as type II diabetes and Parkinson's.

Introduction

The self-association of β-amyloid (Aβ) peptides has been known to be the central event in Alzheimer's Disease (AD) pathogenesis.[1,2] Despite several decades of research on the relationship between Aβ and AD, researchers are still skeptical about the structure–toxicity correlation. Although the recent evidences on Aβ neurotoxicity have shifted the focus towards the toxic oligomers,[3] fibrils which have long been considered as the cause of disease pathogenesis and cannot be ruled out as evidences pertaining to them are still coming along.[4,5] A deeper understanding of the molecular mechanisms and pathways underlying Aβ self-aggregation remains a great challenge to current science. Over the years, independent studies have identified the central (K16-G25) and the C-terminal region (K28-G37) play a vital role in Aβ self-assembly.[2,5,6] Several of these studies have often highlighted a significance of the GxxxG repeating motif from the C-terminus.[7,8] The GxxxG motif is a frequently occurring sequence in trans-membrane proteins and some soluble proteins that contain at least one α-helix.[9] The four residue separation aligns the Gly residues in a GxxxG motif to lie on one face of the helix, and has been reported to stabilize the helix-helix association and the folded state of proteins.[9,10] The lack of side chain in Gly allows the two helices to come into close proximity, and the dimer is thought to be stabilized by van der Waals interactions.[11] The β-branched amino acids such as Ile, Val, and Thr that frequently occurs at the neighboring positions, facilitates Gly to acts as a molecular notch that further strengthens the helix-helix interactions.[11] It has also been reported that AxxxG has a similar effect to the GxxxG motif.[9] Studies have shown that Gly→Leu mutation in these motifs affect amyloid precursor protein dimerization, processing, and subsequent Aβ production.[8] These motifs were suggested to have significant impact on β-sheet formation and the associated neurotoxicity.[7] Before converting into β-sheet, Aβ adopts an antiparallel β-hairpin structure at the $G^{33}LMVG^{37}$ region.[12] Thus, mutation in this segment could favor oligomerization, and subsequent fibrillation. A comprehensive understanding of the system is necessary for a possible structure–function correlation of Aβ pathogenesis. However, the mechanistic insight into this segment-specific aggregation resulting in the structured/unstructured aggregates remains elusive.

Surrounding water molecules have long been acknowledged to be a key player in determining the aggregation propensity of a protein in solution.[13] The hydrogen bond networking with water has a significant influence on the

[a] D. Sarkar, Dr. I. Chakraborty, Dr. A. Bhunia
Department of Biophysics
Bose Institute
P-1/12 CIT Scheme VII (M)
Kolkata 700054 (India)
E-mail: bhunia@jcbose.ac.in
[b] M. Condorelli, Prof. C. La Rosa
Department of Chemical Sciences
University of Catania
95125 Catania (Italy)
E-mail: clarosa@unict.it
[c] B. Ghosh, Dr. A. K Mandal
Division of Molecular Medicine
Bose Institute
P-1/12 CIT Scheme VII (M)
Kolkata 700054 (India)
[d] T. Mass, Dr. M. Weingarth
Department of Chemistry
Utrecht University
Padualaan 8
3584 Utrecht (The Netherlands)
[e] Dr. V. Subramanian
College of Pharmacy
University of Kentucky
Lexington, KY 40536–0596 (USA)
E-mail: vivek.nmr@uky.edu

Supporting information for this article is available on the WWW under https://doi.org/10.1002/cmdc.201900620

Special Collection *This article belongs to the Special Collection "MedChem in India"*

structural stability and dynamics of a protein. Molecular dynamics (MD) simulation studies have indicated that water-mediated interactions can affect the energy landscape of monomers to drive oligomerization.[14] The major driving force behind protofibrilation is being the hydrophobic interaction that facilitates the dehydration of backbone hydrogen bonds i.e. removal of water molecules by the nearby non-polar group which is an entropically driven-process.[15,16] It has also been reported that some of the conformational changes (such as β-sheet) require hydration of the particular segment of peptide chains rather than removal of water.[15] Therefore, in order to gain a deeper understanding of water-peptide interplay in the aggregation propensity of peptides, a detailed investigation of water dynamics will be required.

In this study, we have focused mainly on the C-terminal segment of Aβ peptide to establish a dynamic relationship between toxicity and peptide aggregates. Here, we have designed a 20-residue peptide (namely, AV20), which harbors all the three GxxxG motifs flanked by 3–4 residues on either side (Figure 1A). It should be noted that the flanking residues only provide conformational freedom and ease of study. Additionally, a peptide library was also designed by sequentially and systematically mutating each of these Gly residues to Leu (Figure 1A) in order to understand the role of individual Gly residues in the C-terminal segment of Aβ. Our experiments show that the hydrophobic C-terminal Aβ containing the three repeat GxxxG motifs is evenly neurotoxic. In particular, the $G^{33}xxxG^{37}$ is the primary motif accountable for peptide's neurotoxicity. Moreover, using the solvent relaxation technique we have uncovered the guiding role of water molecules in determining the aggregation propensity of a peptide. It enabled us in discriminating the sequence-dependent mechanism of self-assembly between two peptides.

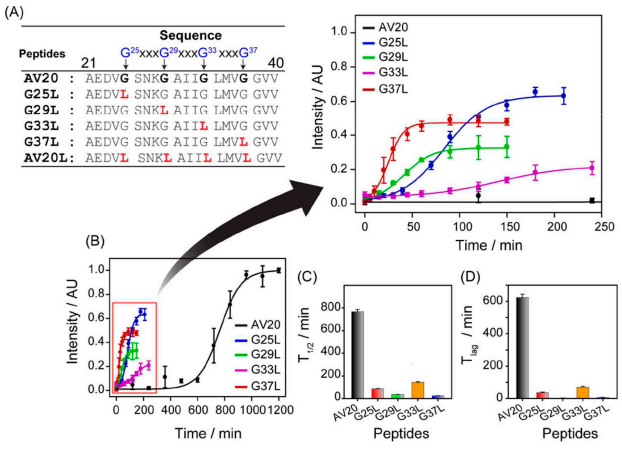

Figure 1. Effect of mutation on aggregation kinetics of AV20. (A) The amino acid sequence of the wild type and the designed mutant peptides. (B) Aggregation kinetics of ~80 μM peptide investigated by ThT based fluorescence assay at 37 °C. All kinetic curves were normalized with respect to AV20. (C–D) The corresponding half-time ($t_{1/2}$) and lag time (t_{lag}) of the aggregation kinetics obtained from Boltzmann fit. All experiments were repeated three times, and the data were averaged (± SD).

Results and Discussion

GxxxG Motifs Modulate Aβ Aggregation Kinetics

The effect of mutation on the aggregation kinetics was evaluated using Thioflavin T (ThT), a β-sheet specific intrinsic dye.[17] The ThT kinetic curves (Figure 1B) were consistent with the secondary nucleation-dominated self-assembling model.[18] The normalized ThT data for each peptide were individually fitted with the secondary nucleation-dominated self-assembling model using the online fitting platform, AmyloFit[19] and the nucleation and elongation rates were obtained thereafter (Table S1). The primary nucleation rate of AV20 was much lower than that of the mutants, whereas we found a varied secondary nucleation and elongation rate profile for the peptide variants. Additionally, the time-dependent ThT kinetic curves were fitted to a sigmoidal growth model[20] to determine the corresponding half-time ($t_{1/2}$) and lag time (t_{lag}) of the aggregation kinetics (Figure 1C–D). AV20 exhibited slower kinetics with a t_{lag} of 622.8 ± 21 min, reaching saturation at ~1200 min of incubation. In contrast, the Gly→Leu mutations dramatically increased the fibrillation rate, resulting in a saturation within 240 min of incubation (Figure 1B). While G25 L displayed a t_{lag} of 36.36 ± 3.80 min, G33 L showed a higher t_{lag} of 69.65 ± 6.63 min with a comparatively low fluorescence intensity at saturation, suggesting a low β-sheet content. G29 L and G37 L displayed almost comparable kinetics, reaching saturation as early as ~120 min. Thus the fine differences observed in the aggregation kinetics among the mutant variants indicated that the positions of these Gly residues also plays a significant role in the aggregation behavior. Due to the insolubility of AV20 L (all Gly mutated), we could not perform any solution state experiments. Nevertheless, the ThT assay indicated a subtle difference in the aggregation behavior between the peptides, which might be a direct consequence of their structural transitions during fibrillation. Confocal microscopy confirmed the time-dependent fibrillation of the wild-type (WT) and mutant peptides (Figure S1). Further, scanning electron microscopy images of the peptide aggregates at their saturation phase confirmed the occurrence of amyloid aggregation (Figure S2). The fibrils exhibited dendritic morphology, consisting of long branched rod-like fibers.[21] While the branching of Aβ40, AV20, G25 L, and G29 L aggregates were random, G33 L and G37 L aggregates were more uniform and linear in nature.

Aggregation Kinetics is Dependent on the Conformational Transitions

Time-dependent Circular Dichroism (CD) spectroscopy was performed to compare the characteristic changes in the secondary conformation during fibrillation (Figure 2A). Initially, all the peptide variants were in random coil conformation (negative band near 195–198 nm). AV20 underwent a structural transition from random coil to β-sheet conformation, via a comparatively stable α-helical intermediate. CD spectra of these intermediates (360 min and 720 min) showed negative bands at 208 nm and 222 nm, characteristic spectral signatures for α-helix and even at saturation

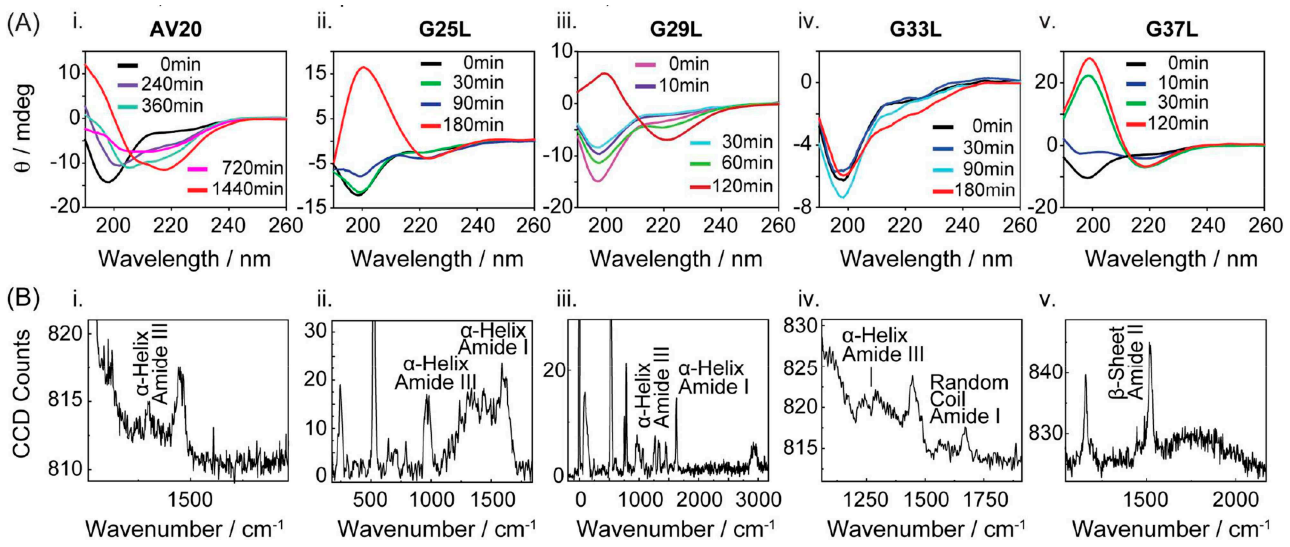

Figure 2. Effect of mutation on the secondary structure of the peptide variants. (A, i–v) Far-UV spectra as a function of time for 80 μM AV20 and the mutant variants showing the time-dependent structural transition from monomer to fibril. The sample contains 80 μM peptide in 20 mM sodium phosphate and 50 mM NaF, pH 7.4. (B, i–v) The SERS spectra of the corresponding peptides at saturation, showing the presence of different secondary structural conformation.

(1440 min), the negative band at 208 nm was visible (Figure 2A,i). However, the predominant band was the negative band at 218 nm, characteristics of β-sheet conformation. Thus, it is most likely that the GxxxG motif maintains a helical conformation so that there exists a dynamic equilibrium between α-helix and β-sheet conformations. Interestingly, such helicalintermediates were not clearly visible in case of mutant peptides. Both G25 L and G29 L underwent comparatively faster structural transition into complete β-sheet conformation (negative bands near 218 nm and positive bands near 198 nm). While, G33 L displayed a small population of β-sheet, G37 L underwent a swift transition from random coil to β-sheet, correlating well with the ThT data. Although fibrils formed by WT and mutant peptides were different at a macroscopic level, solid-state Nuclear Magnetic Resonance (NMR) spectroscopy revealed the presence of β-sheet conformation in the variants.[22] The carbonyl peak ~175 ppm was clearly visible in the corresponding spectra for the tested variants including AV20 L (Figure S3).

Signal Enhanced Raman Spectroscopy (SERS) enabled us to obtain detailed information on the aggregated conformations (Figure 2B).[23] As already reported in other works, SERS spectroscopy can provide an accurate information on secondary structure within 1–2 nm from the nanoparticle (NP) surface.[23] The Raman signal is enhanced lead to the phenomenon of SERS, which decays depending on $1/r^{12}$, where r is the distance between NPs and the molecule.[23] The substrate was obtained by functionalization of Si wafer with silver NPs prepared with a chemical-free synthesis, thus shown the highest enhancement because of their shape and chemical-free surface. AV20 aggregate showed a band centered at 1287 cm^{-1} and 1304 cm^{-1} (amide III) characteristic of a polypeptide backbone in α-helix and β-turn conformation, respectively. Both G25 L and G29 L aggregates showed the presence of α-helix (band at 1631 and 1266 cm^{-1}), β-sheet (1670 and 1248 cm^{-1}) and β-turn (1324 cm^{-1}) secondary structures. Interestingly, SERS spectrum of G33 L showed the presence of random coil structures (amide I band centered at 1672 cm^{-1}), also found in CD spectrum. Both CD and SERS experiments showed strong β-sheet conformation for G37 L aggregates (band centered at 1520 cm^{-1}). Thus, while Gly^{33} mutation exerts a negative effect, Gly^{37} has a stimulatory effect on β-sheet formation.

Atomic Force Microscopy Characterizes the Morphological Differences of the Peptide Aggregates

High-resolution atomic force microscopy (AFM) showed small cylindrical but well-dispersed aggregates for the AV20, where the average longitudinal and vertical lengths were 0.5 ± 0.2 and 0.5 ± 0.1 μm, respectively (Figure 3A). They were spread over a range goes from 0.1-1 μm with an average height of 15 ± 3 nm. Shifting the mutation to Gly25 and Gly29 resulted in more compact and larger aggregates. G25 L aggregates showed an average height increase up to 200 ± 10 nm (transversal) and 110 ± 20 nm (longitudinal) (Figure S4E). G29 L mutant formed oblate aggregates of more ordered structures along a row having an average longitudinal height of 340 ± 100 nm. Surprisingly, while G33 L exhibited unorganized aggregates having an average height of 60 nm, G37 L manifested in highly organized structures with an average height of 220 nm (Figure 3, D–E). In fact, G37 L showed single and continuous fibrillar structures.

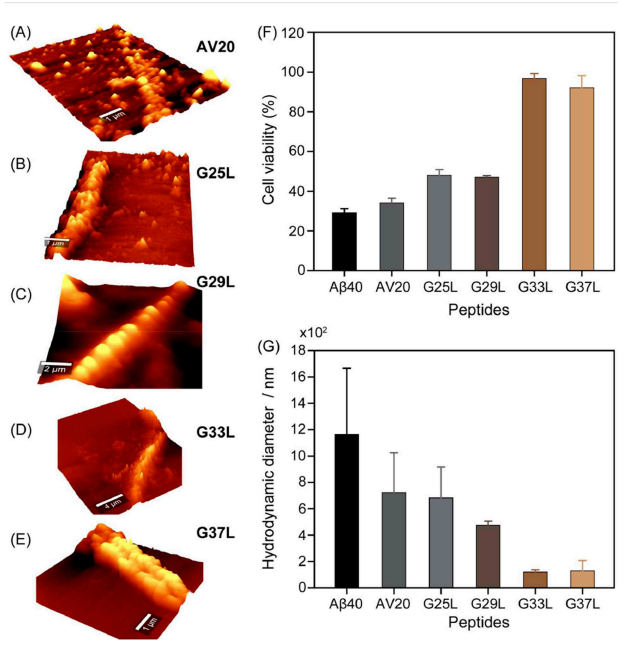

Figure 3. Correlation between aggregation size, morphology, and cytotoxicity. AFM images of (A) AV20, (B) G25 L, (C) G29 L, (D) G33 L, and (E) G37 L peptide aggregates. (F) Cytotoxicity of the tested peptide aggregates (10 μM) against SH-SY5Y cells as obtained from the MTT reduction assay. All experiments were repeated three times, and the data were averaged (± SEM). (G) The hydrodynamic diameters of the peptide variants studied using DLS. The values are average of ten accumulation (± SD).

$G^{33}xxxG^{37}$ Motif Plays the Pivotal Role in Aβ Neurotoxicity

To inspect whether the observed differences in aggregation behaviors are attributed to differences in toxicity, we performed MTT assay with human neuroblastoma SH-SY5Y cells at different timepoints of ThT aggregation kinetics (Figure S5). Interestingly, the cell viability assay depicted a specific structure-toxicity correlation for WT and mutant peptides. AV20 showed a similar toxicity profile when compared with Aβ40 (control), suggesting that the hydrophobic sequence present in the C-terminal fragment of Aβ40 is sufficient for oligomerization and Aβ neurotoxicity. The C-terminus strain of Aβ40 was previously shown to aggregate within lipid bilayers to assume a cone-shaped cross-section, inducing membrane curvature and non-specific ion channel.[24] At saturation, G25 L and G29 L aggregates also showed a high percentage of cytotoxicity (50–60 %), indicating a negligible effect of these mutations on neurotoxicity. Surprisingly, both G33 L and G37 L showed negligible toxicity, signifying that $G^{33}xxxG^{37}$ motif plays a crucial role in Aβ neurotoxicity (Figure 3F). In contrast to the soluble monomeric state with a single conformation, aggregates have an intricate structural landscape allied with multiple aggregate-specific activities.[4]

Aggregate Size and Morphology is Linked with Neurotoxicity

Dynamic light scattering experiment showed a gradual increase in the hydrodynamic diameter of each peptide variants as a function of time (Figure S6). Interestingly, as the mutation shifted towards the C-terminal, the heterogeneity in the aggregate size decreases, also found in AFM images. Particularly, the G33 L and G37 L aggregates were more uniform in size distribution when compared to the other variants. Thus in correlation with the toxicity profile of respective peptides, structural dynamicity can be addressed as an important factor behind neurotoxicity.

Additionally, the unorganized and amorphous nature of G33 L could explain its non-toxicity. In contrast, the equally non-toxic G37 L has a definite β-sheet rich fibril. Moreover, this finding suggested that toxicity and β-sheet fibril are two independent phenomena as also recently suggested.[25] Thus to gain a clearer understanding of the structure–function correlation, we further investigated into the mechanistic pathway that differentiates AV20 and G37 L aggregation.

Thermal Stability and Solvent Dynamics Plays a Crucial Role in Determining the Aggregation Propensity and Pathway

The thermal stability of peptide's secondary structures was investigated by a temperature-induced folding-unfolding study.[26] For this, CD experiments were performed for AV20 and G37 L at different temperatures (Figure 4A, B). AV20 showed a minimal effect on the secondary conformation. The absorbance (θ) at 218 nm versus temperature plot showed an unstable partial β-sheet conformation (Figure 4A, inset). However, G37 L developed a complete β-sheet structure which remained stable up to 90 °C (Figure 4B, inset), suggesting that Leu mutation stabilizes inter-chain hydrophobic contacts[27] and that the C-terminal region plays a pivotal role in fibril formation according to AFM data. Moreover, the temperature-dependent CD data indicates that G37 L is more aggregation prone than AV20. These datasets were analyzed using singular value decomposition (SVD)[28] to determine the minimum number of spectroscopically distinct species during temperature-dependent structural transition. The number of principle components (PC), which represents the number of distinct structural species in the dataset, can be estimated by taking into account of (i) the significance of singular values (Figures 4 C–D), and (ii) smooth shape of the v_i vectors (Figures 4 E–F). Both AV20 and G37 L showed that the primary two components have smooth shape that corresponds to the singular values with the highest magnitude. Thus the results of SVD analysis suggested that the temperature-dependent structural transition is a two-step process in either case. While, Figures 4G, H represents the left singular vectors corresponding to the 1st two components of AV20 and G37 L, respectively (the spectral shapes), the right singular vectors contains the amplitudes of each component (1st five components) as a function of temperature (Figures 4 E–F). Thus, in correlation with the left singular value plots, the right singular vector plots indicates a partial β-sheet conformation of AV20 with increasing the temperature. It is worth mentioning that the amount of random coil remained almost same (Figure 4E).

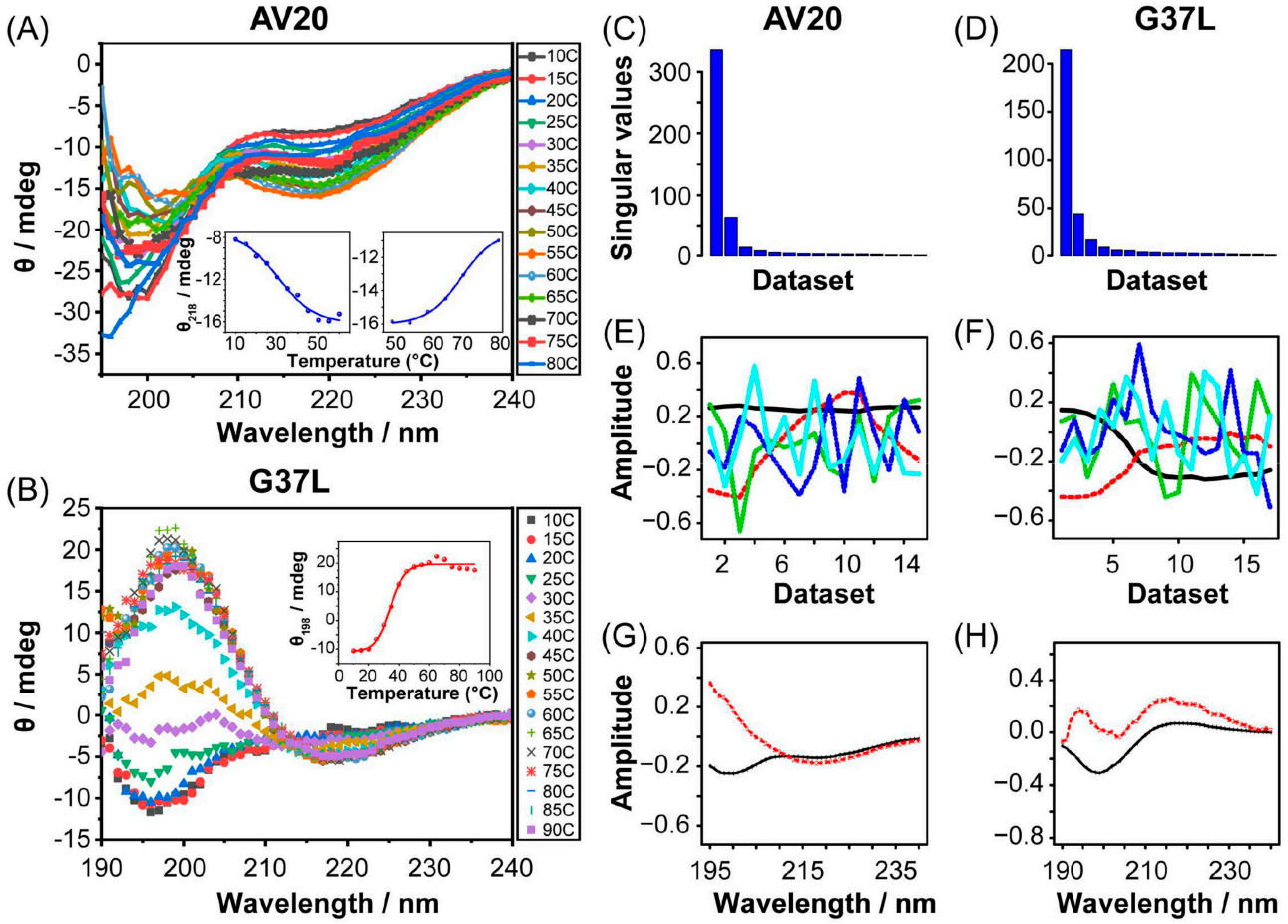

Figure 4. The temperature-dependent CD spectroscopy for (A) AV20, and (B) G37 L. Inset images of (A) show the absorbance (θ) versus temperature plot at 218 nm. The plots were fitted using the Boltzmann equation. Inset image of (B) shows the same plot at 198 nm for G37 L. In (C) and (D), blue-bars show the singular values in descending order, for AV20 and G37 L, respectively. (E), and (F) represent the shape of the v_i vectors for the first five components plotted against the number of temperatures taken for AV20 and G37 L respectively. The primary two components have a smooth shape that corresponds to the singular values with the highest magnitude. (G), and (H) are the first two u_i vectors corresponding to the principal components for AV20 and G37 L, respectively.

To gain an atomic-resolution insight into this temperature-dependent structural change, 1D ^{1}H NMR spectra were recorded for AV20 and G37 L (Figure S7). The chemical shift changes in the amide proton as a function of temperature have been used to examine the strength of hydrogen bond or the formation of intramolecular hydrogen bond.[29] The results of temperature-dependent 1D ^{1}H NMR spectra of the peptide tested here showed that all amide peaks exhibited a temperature-dependent displacement of their chemical shifts in up-field direction. Distinct 1D peaks of AV20 were identified from 2D ^{1}H-^{1}H total correlation spectroscopy (TOCSY) and rotating frame Overhauser spectroscopy (ROESY) experiments (Figure S8). The temperature coefficient for these distinct peaks were calculated by plotting the amide proton chemical shift as a function of temperature, over the temperature range of 283 to 310 K. The coefficients for AV20 suggested probable intramolecular hydrogen-bonding, resulting in a partial conformational uptake.[30] In contrast, G37 L manifested in a very high negative temperature coefficient, corroborating well with its β-sheet pre-disposition. Apart from the observed amide proton chemical shift changes, a temperature-dependent line-broadening was also apparent. The line broadening rate was higher for G37 L, suggesting a higher amide proton exchange with solvent molecule (Figure S7). The line broadening could also arise from the fact that the G37 L peptide is more aggregation prone than AV20 at higher temperatures (Figure 4). Moreover, this further confirms the possible role of the adjacent solvent molecules in aggregation.

It is noteworthy to mention that in an aqueous solution, the water molecules directly attached to specific sites on the protein via intermolecular H-bonding are termed as the "bound" fraction (slower rotational motion), whereas the fast rotating bulk water molecules remain as the "free" fraction.[31] During fibrillation, the decrease or the increase of the "bound" fraction in the solution may affect the magnitude of the observed transverse relaxation time (T_2) of water (Equation 3 in SI). Based on this hypothesis, the peptide-solvent interactions during aggregation were monitored using an efficient adaptation of solvent relaxation NMR technique.[32] This technique measured the T_2 of water using a Carr-Purcell-Meiboom-Gill

(CPMG)[33] sequence (Figure S9) at different time points in the aggregation pathway. So we performed the solvent relaxation experiments of both the peptides AV20, and G37 L and the solvent relaxation behavior for the two peptides showed distinct water dynamics during fibrillation (Figure 5). This dual nature of T_2s versus time plots can be satisfactorily explained by the previously proposed model.[34] At 37 °C the T_2s for solvent molecules associated with AV20 initially decreased as a result of an entropy-driven water exclusion that catalyzes hydrophobic interactions. This, probably drives the system to change its conformation from random coil to α-helix,[15] as was previously seen using CD spectroscopy. During nucleus formation, α-helix compacts the chain via intra-segment hydrogen bonding and an intense van der Waals contact, in the expense of gaining translational entropy through expelling water.[35] This was followed by a gradual increase in T_2 after ~240 min of incubation (Figure 5A), as a significant population of the peptide begins to convert into β-sheet. This phenomenon is expected to be dominantly mediated by increased hydration of the polypeptide chains with subsequent ordering of water molecules on the surface.[16,34,36] The transition from α-helix to β-sheet is manifested by a sequential rearrangement of the hydrophilic side-chains to orient outwardly, facilitating intermolecular interactions with solvent molecules.[14,37] The slower exchange rate with solvent water as a result of β-sheet formation may also contribute to the escalation of T_2.[38] Interestingly, G37 L displayed no systematic change in T_2 values at 37 °C, possibly due to the fast saturation upon rapid β-sheet formation (Figure 5B, inset). Even at a lower temperature (as low as 18 °C and 10 °C) where the kinetics is expected to be slower and comparable with the NMR time scale, G37 L revealed a constant increase in the T_2 values reaching saturation as early as ~180 min (Figure 5B, Figure S10). Thus the Gly→Leu mutation either destabilizes the formation of helical intermediates resulting in a direct conversion into β-sheet structure or in a very fast transition into β-sheet that could not be detected in the NMR timescale.

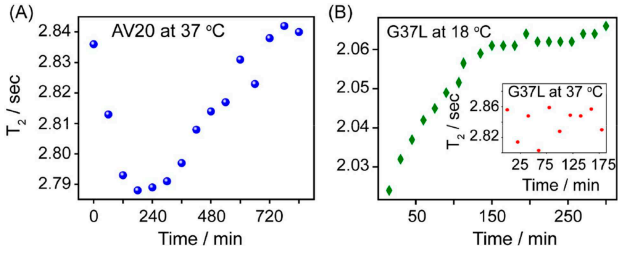

Figure 5. Solvent relaxation. (A) The transverse relaxation time of water measured at 37 °C of AV20 solution plotted as a function of time. (B) The transverse relaxation time of water in G37 L solution plotted as a function of time measured at 18 °C, and 37 °C (inset). The marker-size in each plot denotes the error in the measurement of T_2, which is in order of 10^{-3} (FiFigure 4
gure S11).

Conclusions

This study demonstrates the uniqueness of the GxxxG repeating motifs in the WT (AV20) peptide in maintaining structural dynamicity and subsequent neurotoxicity. Previous NMR studies on Aβ40 have shown that the solvent accessible turns at Gly^{25}-Gly^{29} and Gly^{37}-Gly^{38} facilitate the compact foldings of the peptide.[39] In association with the adjacent β-branched residues (Ile and Val), Gly acts as a molecular notch facilitating the wild-type helix-helix interactions.[11] Mutation in these crucial structural motifs modulates the hydrogen bond networking that affects the helix-helix association, mediating in differential pathways of fibrillation. The solvent relaxation studies, further, proved as an effective strategy to differentiate between the aggregation pathways, giving an in-depth mechanistic insight. Our results indicate that the toxicity of the mutants decreases until it vanishes as the substitution with Leu moves closer to the C-terminal. The GxxxG motif contributes to the flexibility and subsequent conformational heterogeneity of the WT peptide, as suggested by the fast transition from random coil to β-sheet intermediates and the lack of intermediate α-helical conformations for Gly mutants. Thus, the enhanced structural heterogeneity observed for the GxxxG motif ranks in accordance with the observed cytotoxicity.

Theoretical models have suggested that the hydrogen bonding between the C=O and H-C_α of two contiguous chains facilitate the formation of a lock that stabilizes the membrane-compromising conformation of Aβ40.[24,39] Moreover, the conformational selection is in part driven by hydrogen bonding networks. Gly→Leu mutation destabilizes this conformer by preventing the hydrogen bond formation, reducing the neurotoxicity. Conversely, Gly being non-chiral and with a very small side-chain has many degrees of freedom rendering an advantage to the WT peptide enabling successful insertion across the membrane through pore formation. Our data strongly agree with recent studies where just one stereoisomer of silybin inhibit Aβ40 toxicity by binding the C-terminal hydrophobic segment 35–40.[40] This would enable the designing of novel inhibitors against Aβ40/42 to aid in targeted therapy of neurotoxic Alzheimer's and other related diseases, such as type II diabetes and Parkinson since amylin and α-synuclein show the similar SxxxG or GxxxG/GxxxxG repeat motif, respectively.

Experimental Section

Sample Preparation

Chemicals and solvents were obtained from Sigma Aldrich, USA. Synthetic unlabeled peptides were purchased from GenScript (Piscataway, USA) and GL Biochem (Shanghai, China) (Figure 1A). The purity of the peptides was checked by HPLC and mass spectra (data not shown). The peptides were dissolved in 5% NH_4OH, vortex well and kept at 4 °C for 1 h followed by a lyophilization. A stock solution of desired concentration was prepared by dissolving the lyophilized peptide in 20 mM phosphate buffer, 50 mM NaCl (pH 7.4, 0.01% sodium azide).

Aggregation Kinetics Experiment by Thioflavin T (ThT) Fluorescence Assay

We performed ThT fluorescence assay to study the kinetics of amyloid aggregation. Stock solutions of ~80 μM peptide concentration for wild type (WT) and mutant peptides were prepared in the buffer mentioned above, followed by a three minute of ultrasonication and then incubated at 37 °C temperature under a shaking condition. All fluorescence measurements were carried out in Hitachi F-7000 FL spectrometer at various time points of aggregation with an excitation wavelength of 440 nm, emission range of 460–520 nm, using 5 nm slit width for both excitation and emission. Three independent experiments were performed throughout with maximum delay time of 5 min for sample preparation. Time-dependent ThT fluorescence data were normalized and fitted to a sigmoidal growth model[20] where the half-life $t_{1/2}$ is the time required to reach half of the fluorescence intensity, b is the apparent first-order constant and Y_{max}, and Y_0 are, respectively, the maximum and initial fluorescence values:

$$Y = Y_0 + (Y_{max} - Y_0)/(1 + \exp((t - t_{1/2}/b)) \quad (1)$$

The lag time (t_{lag}) of amyloid kinetics was determined as ($t_{1/2} - b$). To obtain the nucleation and elongation rates, we performed individual fits to the normalized ThT data for each peptide using the online fitting platform AmyloFit.[19]

Confocal Microscopy

At different time intervals, aliquots of each peptide incubations were diluted to 10 μM final concentration. After the addition of 20 μM ThT in each aliquot, 10 μL sample mixer was placed on a glass slide. After air-drying, samples were mounted with Dibutyl phthalate Polystyrene Xylene (DPX), and the images were taken using a 63× objective in oil immersion in a confocal microscope (Leica TCSSP8 and the LAS AF Version 2.1.0 built-in 4316 software, Leica Microsystems GmbH, Germany).

Scanning electron Microscopy (SEM)

Aliquots of each peptide solution were taken at the time of saturation phase and deposited on a glass slide followed by overnight air-drying. The slides were then coated with gold for 120 s at 10 kV voltage and 10 mA current. The sample images were recorded using a ZEISS EVO-MA 10 scanning electron microscope equipped with a tungsten filament gun operating at 10 kV.

Circular Dichroism (CD) Spectroscopy

CD measurements were taken on a JASCO J-1500 CD spectrometer using a 0.1 cm path length cell with a slit width of 2 nm. WT and mutant peptides of ~80 μM concentration were prepared in 20 mM phosphate buffer, 50 mM NaF (pH 7.4) and incubated at 37 °C under shaking condition. At different time intervals, Far-UV CD spectra were recorded at 25 °C, from 260 nm to 190 nm with a scan speed of 100 nm/min. Temperature-dependent CD spectra were recorded for AV20 (10–80 °C) and G37 L (10–90 °C). For each spectrum, five readings were taken (i.e., five accumulations), and the average was considered. Smoothing and buffer subtraction was done for processing of raw data, as per the manufacturer's recommendation.

Surface-Enhanced Raman Spectroscopy (SERS)

The (powder form) peptides were dissolved in 5% ammonium hydroxide, vortex well and kept at 4 °C for 1 h followed by lyophilization. A stock solution of 80 μM peptide concentration was prepared by dissolving the lyophilized peptide in 20 mM phosphate buffer, 50 mM NaCl (pH 7.4, 0.01% sodium azide) and incubated at 37 °C under shaking condition (250 rpm). Fibrillation time for AV20 was 24 h, and for G25 L, G29 L, G33 L, and G37 L was 180 min. After the incubation, aliquots of stock solution were diluted in phosphate buffer to obtain 8 μM solutions. The solutions thus prepared were analyzed by Raman spectroscopy using a 532 nm Laser with 10 accumulations and an exposition time of 10 seconds in back-scattering mode.

Atomic Force Microscopy (AFM)

For AFM experiment, the sample aggregates were prepared as described above in SERS. AFM analysis was done by operating in contact mode with an etched-silicon probe with a pyramidal-shape tip having a nominal curvature of 10 nm and a nominal internal angle of 35°; the height images were obtained by scanning 512× 512 points. A Witec Alpha 300 RS instrument was used for both analyses.

MTT Assay

Human neuroblastoma SH-SY5Y cells were grown in DMEM culture media supplemented with 10% FBS. Cells were then harvested using trypsin and counted using a hemocytometer. 5×10^3 cells/well were seeded in 96 well cell culture plates. At 70% confluence, the cells were treated with Aβ40, AV20, G25 L, G29 L, G33 L, and G37 L at concentrations of 10 μM and 40 μM as a function of time for 24 hours. The media was then discarded, and cells were treated with 3-(4, 5-dimethylthiazol-2-yl)-2, 5-diphenyltetrazolium bromide (MTT reagent) and incubated at 37 °C for 4 h. After incubation, the MTT reagent was replaced by MTT solvent DMSO and kept at room temperature for 15 min. Absorbance was measured at OD-590 nm.

Dynamic Light Scattering (DLS)

DLS measurements were carried out to determine the hydrodynamic diameter of various species throughout the aggregation process, using Malvern Zetasizer Nano S (Malvern Instruments, UK) equipped with a 4 mW He–Ne gas laser (beam wavelength = 632.8 nm) and 173° back scattering measurement facility. All peptides were taken for fibrillation by the same process as mentioned in the ThT fluorescence assay. Measurements were taken for 10 μM peptide concentration at different timepoint if aggregation using low volume disposable sizing cuvette. The *Z*-average diameter was calculated from the correlation function using Malvern technology software.

NMR Spectroscopy

All experiments were performed using Bruker Avance III 500 MHz NMR spectrometer equipped with a 5 mm SMART probe or on a Bruker Avance III 700 MHz NMR spectrometer, equipped with a RT probe. To the sample solution of 600 μL final volume, 10% D_2O was added along with TSP (Trimethylsilylpropionic acid) as a reference for all the NMR experiments performed. Two-dimensional ^{1}H-^{1}H total correlation spectroscopy (2D TOCSY) and two-dimensional ^{1}H-^{1}H rotating frame Overhauser spectroscopy (2D ROESY) were recorded for the free AV20 at 15 °C, with a mixing time of 80 ms and 250 ms, respectively. Total number of scans for TOCSY and

ROESY were 48 and 64, respectively. Data processing and analysis were carried out using Topspin™ v3.2 software (Bruker Biospin, Switzerland) and Sparky (https://www.cgl.ucsf.edu/home/sparky) software, respectively.

Temperature-dependent 1D ^{1}H NMR experiments were performed for AV20 and G37 L at different temperatures (10 °C, 15 °C, 20 °C, 25 °C, 30 °C, and 37 °C). For the solvent relaxation experiments, AV20 and G37 L sample solutions were prepared at a concentration of 160 μM where the solvent composition was 10% D_2O and 90% H_2O (v/v). To study the solvent isotope effect, we used the same sample concentration dissolved in the solvent with 40% D_2O and 60% H_2O (v/v).

Solid-state NMR ^{13}C cross-polarization spectra of AV20, AV20 L, G33 L, and G37 L peptide aggregates were acquired at 500 MHz (^{1}H frequency), 10 kHz magic angle spinning, and natural isotope abundance. The contact time was 0.5 ms and the interscan delay 1.8 s. The amplitude of the 90° pulse on the proton channel was 80 kHz. For each sample, we manually packed 3 mg of lyophilized powder peptide directly packed in 3.2 mm rotors and the spectra were acquired with 35840 scans.

Solvent Relaxation NMR

Transverse relaxation rates of solvent water were measured using CPMG with 8 π pulse block (Figure S9), where the block-time (T) for all the experiments was set at 10 ms. In the case of AV20 peptide, the temperature was fixed at 37 °C. This temperature was chosen in such a way that the timescale of the aggregation for this peptide would be quite compatible with the NMR timescale. In case of G37 L, the entire set of solvent relaxation experiments were performed at three different temperatures. At 37 °C, it undergoes fibrillation very rapidly compared to NMR timescale. The other two temperatures were kept fixed at 18 °C and 10 °C, where it is expected to aggregate slowly within NMR time-regime. The recycle delay for every experiment was 35 s. As the signal to noise ratio is very high in case of water peak, only a single scan was used for every relaxation experiment to minimize the experimental time to record a single T_2. All raw data were processed by a script written using Julia version 0.6.2. The peak intensities were fit with Lorentzian and Gaussian functions where the fitting correlation in each case was nearly 0.999. T_2s were extracted from the single-exponential fit of deconvoluted echo-intensities of water peak versus time (Figure S11). The extracted T_2s were plotted against time.

Singular Value Decomposition (SVD) Analysis

Temperature-dependent CD data for AV20 and G37 L were subjected to SVD analysis. The equation for singular value decomposition of A is as follows[41]:

where U is an M×N matrix whose columns are the left singular vectors, u_i (wavelength coefficient vectors); S is an N×N diagonal matrix, whose elements are called singular values, s_i; and V^T (transpose of V matrix) is also an N×N matrix, whose rows are the right singular vectors, v_i (temperature coefficient vectors).

Here, U represents the basis spectra (the spectral shapes) that make up the data set, and V contains the amplitudes of each component as a function of temperature. SVD analysis and subsequent plots have been done using the statistical R package (R Development Core Team, 2005, https://www.r-project.org/).

Acknowledgements

This work was supported in part by the Council of Scientific and Industrial Research (02(0292)/17/EMR-II to A.B.) and partly by the Bose Institute intramural external research fund (R/16/19/1615 to A.B.), Government of India. C.L.R. and M.C. are grateful to PON project Bionanotech, Research and Innovation Tower (BRIT) financed by the Italian Ministry for Education, University and Research (MIUR). D.S. thanks the Department of Science and Technology, Government of India, for JRF. I.C. acknowledges Dr. Rangeet Bhattacharyya for water relaxation experiments. Thanks to Dr. Sylvie Garneau-Tsodikova for critical reading of the manuscript.

Keywords: β-amyloid · toxicity · CD · Raman spectroscopy · AFM · solvent relaxation NMR

[1] S. J. Lee, E. Nam, H. J. Lee, M. G. Savelieff, M. H. Lim, *Chem. Soc. Rev.* **2017**, *46*, 310–323; P. C. Ke, M. A. Sani, F. Ding, A. Kakinen, I. Javed, F. Separovic, T. P. Davis, R. Mezzenga, *Chem. Soc. Rev.* **2017**, *46*, 6492–6531; N. L. Fawzi, D. S. Libich, J. Ying, V. Tugarinov, G. M. Clore, *Angew. Chem. Int. Ed. Engl.* **2014**, *53*, 10345–10349; J. Hardy, D. J. Selkoe, *Science* **2002**, *297*, 353–356; S. I. Cohen, S. Linse, L. M. Luheshi, E. Hellstrand, D. A. White, L. Rajah, D. E. Otzen, M. Vendruscolo, C. M. Dobson, T. P. Knowles, *Proc. Natl. Acad. Sci. USA* **2013**, *110*, 9758–9763.

[2] R. Ahmed, G. Melacini, *Chem. Commun. (Camb.)* **2018**, *54*, 4644–4652.

[3] T. L. Lau, J. D. Gehman, J. D. Wade, K. Perez, C. L. Masters, K. J. Barnham, F. Separovic, *Biochim. Biophys. Acta* **2007**, *1768*, 2400–2408; M. Sakono, T. Zako, *FEBS J.* **2010**, *277*, 1348–1358.

[4] N. Itoh, E. Takada, K. Okubo, Y. Yano, M. Hoshino, A. Sasaki, M. Kinjo, K. Matsuzaki, *ChemBioChem* **2018**, *19*, 430–433.

[5] T. Okada, M. Wakabayashi, K. Ikeda, K. Matsuzaki, *J. Mol. Biol.* **2007**, *371*, 481–489; R. Ahmed, M. Akcan, A. Khondker, M. C. Rheinstädter, J. C. Bozelli, R. M. Epand, V. Huynh, R. G. Wylie, S. Boulton, J. Huang, C. P. Verschoor, G. Melacini, *Chem. Sci.* **2019**, *10*, 6072–6082; R. Cascella, M. Perni, S. W. Chen, G. Fusco, C. Cecchi, M. Vendruscolo, F. Chiti, C. M. Dobson, A. De Simone, *ACS Chem. Biol.* **2019**, *14*, 1352–1362.

[6] J. T. Jarrett, E. P. Berger, P. T. Lansbury, *Biochemistry* **1993**, *32*, 4693–4697; L. O. Tjernberg, D. J. Callaway, A. Tjernberg, S. Hahne, C. Lilliehöök, L. Terenius, J. Thyberg, C. Nordstedt, *J. Biol. Chem.* **1999**, *274*, 12619–12625; J. R. Brender, A. Ghosh, S. A. Kotler, J. Krishnamoorthy, S. Bera, V. Morris, T. B. Sil, K. Garai, B. Reif, A. Bhunia, A. Ramamoorthy, *Chem. Commun. (Camb.)* **2019**, *55*, 4483–4486; S. Bera, E. Arad, L. Schnaider, S. Shaham-Niv, V. Castelletto, Y. Peretz, D. Zaguri, R. Jelinek, E. Gazit, I. W. Hamley, *Chem. Commun. (Camb.)* **2019**, *55*, 8595–8598.

[7] A. Harmeier, C. Wozny, B. R. Rost, L. M. Munter, H. Hua, O. Georgiev, M. Beyermann, P. W. Hildebrand, C. Weise, W. Schaffner, D. Schmitz, G. Multhaup, *J. Neurosci.* **2009**, *29*, 7582–7590; L. W. Hung, G. D. Ciccotosto, E. Giannakis, D. J. Tew, K. Perez, C. L. Masters, R. Cappai, J. D. Wade, K. J. Barnham, *J. Neurosci.* **2008**, *28*, 11950–11958.

[8] L. M. Munter, P. Voigt, A. Harmeier, D. Kaden, K. E. Gottschalk, C. Weise, R. Pipkorn, M. Schaefer, D. Langosch, G. Multhaup, *EMBO J.* **2007**, *26*, 1702–1712.

[9] G. Kleiger, R. Grothe, P. Mallick, D. Eisenberg, *Biochemistry* **2002**, *41*, 5990–5997.

[10] W. P. Russ, D. M. Engelman, *J. Mol. Biol.* **2000**, *296*, 911–919.

[11] A. Senes, M. Gerstein, D. M. Engelman, *J. Mol. Biol.* **2000**, *296*, 921–936.

[12] M. Decock, S. Stanga, J. N. Octave, I. Dewachter, S. O. Smith, S. N. Constantinescu, P. Kienlen-Campard, *Front Aging Neurosci* **2016**, *8*, 107.

[13] K. A. Dill, *Biochemistry* **1990**, *29*, 7133–7155.

[14] S. H. Chong, S. Ham, *Angew. Chem. Int. Ed. Engl.* **2014**, *53*, 3961–3964.

[15] D. Thirumalai, G. Reddy, J. E. Straub, *Acc. Chem. Res.* **2012**, *45*, 83–92.

[16] U. Novak, J. Grdadolnik, *J. Mol. Struct.* **2017**, *1135*, 138–143.

[17] D. Bhattacharyya, R. Kumar, S. Mehra, A. Ghosh, S. K. Maji, A. Bhunia, *Chem. Commun. (Camb.)* **2018**, *54*, 3605–3608; M. Biancalana, S. Koide, *Biochim. Biophys. Acta* **2010**, *1804*, 1405–1412; R. Cukalevski, X. Yang, G. Meisl, U. Weininger, K. Bernfur, B. Frohm, T. P. J. Knowles, S. Linse, *Chem.*

Sci. **2015**, *6*, 4215–4233; G. Meisl, X. Yang, C. M. Dobson, S. Linse, T. P. J. Knowles, *Chem. Sci.* **2017**, *8*, 4352–4362.
[18] M. Törnquist, T. C. T. Michaels, K. Sanagavarapu, X. Yang, G. Meisl, S. I. A. Cohen, T. P. J. Knowles, S. Linse, *Chem. Commun. (Camb.)* **2018**, *54*, 8667–8684.
[19] G. Meisl, J. B. Kirkegaard, P. Arosio, T. C. Michaels, M. Vendruscolo, C. M. Dobson, S. Linse, T. P. Knowles, *Nat. Protoc.* **2016**, *11*, 252–272.
[20] P. Arosio, T. P. Knowles, S. Linse, *Phys. Chem. Chem. Phys.* **2015**, *17*, 7606–7618.
[21] A. Ghosh, A. S. Pithadia, J. Bhat, S. Bera, A. Midya, C. A. Fierke, A. Ramamoorthy, A. Bhunia, *Biochemistry* **2015**, *54*, 2249–2261.
[22] B. Chandra, D. Bhowmik, B. K. Maity, K. R. Mote, D. Dhara, R. Venkatramani, S. Maiti, P. K. Madhu, *Biophys. J.* **2017**, *113*, 805–816; M. Rad-Malekshahi, K. M. Visscher, J. P. Rodrigues, R. de Vries, W. E. Hennink, M. Baldus, A. M. Bonvin, E. Mastrobattista, M. Weingarth, *J. Am. Chem. Soc.* **2015**, *137*, 7775–7784.
[23] L. D'Urso, M. Condorelli, O. Puglisi, C. Tempra, F. Lolicato, G. Compagnini, C. La Rosa, *Phys. Chem. Chem. Phys.* **2018**, *20*, 20588–20596.
[24] M. Pannuzzo, D. Milardi, A. Raudino, M. Karttunen, C. La Rosa, *Phys. Chem. Chem. Phys.* **2013**, *15*, 8940–8951.
[25] F. Scollo, C. Tempra, F. Lolicato, M. F. Sciacca, A. Raudino, D. Milardi, C. La Rosa, *J. Phys. Chem. Lett.* **2018**, *9*, 5125–5129.
[26] G. Malgieri, G. D'Abrosca, L. Pirone, A. Toto, M. Palmieri, L. Russo, M. F. M. Sciacca, R. Tatè, V. Sivo, I. Baglivo, R. Majewska, M. Coletta, P. V. Pedone, C. Isernia, M. De Stefano, S. Gianni, E. M. Pedone, D. Milardi, R. Fattorusso, *Chem. Sci.* **2018**, *9*, 3290–3298.
[27] K. P. Murphy, E. Freire, in *Advances in protein chemistry, Vol. 43*, Elsevier, **1992**, pp. 313–361.
[28] I. Wang, S. Y. Chen, S. T. Hsu, *Sci. Rep.* **2016**, *6*, 31514.
[29] F. J. Blanco, G. Rivas, L. Serrano, *Nat. Struct. Biol.* **1994**, *1*, 584–590.
[30] K. Gademann, B. Jaun, D. Seebach, R. Perozzo, L. Scapozza, G. Folkers, *Helv. Chim. Acta* **1999**, *82*, 1–11.
[31] N. Nandi, B. Bagchi, *J. Phys. Chem. B* **1997**, *101*, 10954–10961; A. De Simone, G. G. Dodson, C. S. Verma, A. Zagari, F. Fraternali, *Proc. Natl. Acad. Sci. USA* **2005**, *102*, 7535–7540.
[32] C. L. Cooper, T. Cosgrove, J. S. van Duijneveldt, M. Murray, S. W. Prescott, *Soft Matter* **2013**, *9*, 7211–7228.
[33] H. Y. Carr, E. M. Purcell, *Phys. Rev.* **1954**, *94*, 630.
[34] I. Chakraborty, K. Mukherjee, P. De, R. Bhattacharyya, *J. Phys. Chem. B* **2018**, *122*, 6094–6100.
[35] L. Cruz, B. Urbanc, J. M. Borreguero, N. D. Lazo, D. B. Teplow, H. E. Stanley, *Proc. Natl. Acad. Sci. USA* **2005**, *102*, 18258–18263; L. Pauling, R. B. Corey, H. R. Branson, *Proc. Natl. Acad. Sci. USA* **1951**, *37*, 205–211.
[36] Y. Fichou, G. Schirò, F. X. Gallat, C. Laguri, M. Moulin, J. Combet, M. Zamponi, M. Härtlein, C. Picart, E. Mossou, H. Lortat-Jacob, J. P. Colletier, D. J. Tobias, M. Weik, *Proc. Natl. Acad. Sci. USA* **2015**, *112*, 6365–6370.
[37] R. K. Kar, J. R. Brender, A. Ghosh, A. Bhunia, *J. Chem. Inf. Model.* **2018**, *58*, 1576–1586.
[38] I. Kheterpal, S. Zhou, K. D. Cook, R. Wetzel, *Proc. Natl. Acad. Sci. USA* **2000**, *97*, 13597–13601.
[39] M. Ahmed, J. Davis, D. Aucoin, T. Sato, S. Ahuja, S. Aimoto, J. I. Elliott, W. E. Van Nostrand, S. O. Smith, *Nat. Struct. Mol. Biol.* **2010**, *17*, 561–567.
[40] M. F. Sciacca, V. Romanucci, A. Zarrelli, I. Monaco, F. Lolicato, N. Spinella, C. Galati, G. Grasso, L. D'Urso, M. Romeo, *ACS Chem. Neurosci.* **2017**, *8*, 1767–1778.
[41] V. Klema, A. Laub, *IEEE Trans. Autom. Control* **1980**, *25*, 164–176.

Manuscript received: November 4, 2019
Revised manuscript received: November 19, 2019
Accepted manuscript online: November 24, 2019
Version of record online: December 3, 2019